International Journal of Computer Information Systems and Industrial Management Applications
ISSN 2150-7988 Volume 18(16s) 2026 pp. 1182-1203
https://doi.org/10.70917/ijcisim-2026-4647
Article

Fiber Bragg Grating Sensors for Temperature and Strain Monitoring: Simulation-Based Analysis of Quasi-Distributed Configurations

Shivprakash Palhewar*[1], Anubhuti Khare[2]

*[1]Research Scholar, Dept. of Electronics and Communication Engineering, RGPV, Bhopal, India
[2]Dept. of Electronics and Communication Engineering, RGPV, Bhopal, India
Corresponding author: sp.sahu49@gmail.com

Abstract: Fiber Bragg Grating (FBG) sensor is one of the most mature wavelength encoded precision measurement transducers, which has the advantage of immunity to electromagnetic disturbance, millimetre-level sensing scale and the ability to mount many independent sensing nodes on a single fibre. In this paper, a simulation study of the FBG sensors and their quasi-distributed configuration has been performed in OptiSystem, in which the sensors are used for both temperature and axial strain monitoring. The first FBG is a uniform FBG with a grating length of 10 mm, and its Bragg wavelength, total output power, noise power and signal to noise ratio (SNR) are measured as the temperature and axial strain are sequentially applied in the range of 30 °C to 210 °C and the range of 1 με to 9 με, respectively. This model is then replicated in a four-element quasi-distributed network consisting of four FBGs positioned at 1545, 1550, 1555 and 1560 nm, and multiplexed and interrogated serially with wavelength division multiplexing (WDM) across three separate sensing locations, with a co-located temperature–strain grating pair included at the third sensing location to enable cross-sensitivity discrimination. The point sensor has a linear thermal response of ~14.2 pm/°C and a linear strain response of ~1.2 pm/με, which is in good agreement with the thermo-optic and elasto-optic models. The quasi-distributed network generates four completely separated spectral channels (no measurable inter-channel overlap) at a channel spacing of 5 nm, and ensures wavelength traceability at each node. The four gratings are represented on a three-span girder bridge to show how the simulated channel plan is translated into an instrumentation layout for structural health monitoring, and how the extracted sensitivities are compared with experimental and numerical results reported.
Keywords: Fiber Bragg Grating (FBG); quasi-distributed sensing; wavelength division multiplexing (WDM); temperature sensing; strain sensing; apodization; OptiSystem simulation; Bragg wavelength shift; signal-to-noise ratio; structural health monitoring; bridge instrumentation

1. Introduction

Optical fibre sensors possess a combination of properties that are not matched by conventional electromechanical transducers: immunity to electromagnetic interference (EMI), small cross-section, which allow embedding in host materials, high sensitivity, chemical inertness, long-term stability and the possibility of embedding many sensing elements in a single fibre strand for multiplexing [1], [2]. The optical fibre sensors are well suited for deployment in applications that are hostile to traditional electrical sensing such as power generation plants, chemical processing plants, aerospace structures, tunnels and ageing civil infrastructure.

There are several separate axes with respect to which the family of optical fibre sensors can be arranged, as summarised in Fig. 1. Sensors can be characterized according to how the optical property of the measurand is modulated (intensity, phase, wavelength or polarization), whether transduction takes place in the intrinsic region of the sensor or in the extrinsic region, and most importantly for the present work, by the extent in space over which the measurand is sampled.

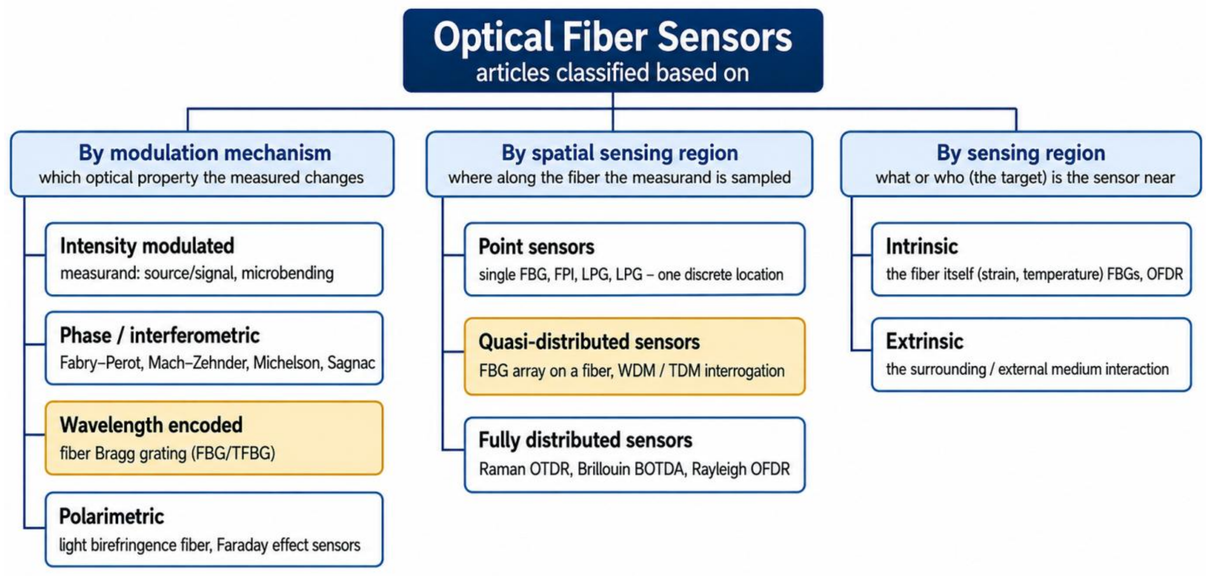

Fig. 1. Classification of optical fibre sensor types, with the branches addressed in this study shaded.

In the point-sensor branch, the main families of devices are Fabry–Pérot interferometers (FPI), Mach–Zehnder interferometers (MZI), long-period fibre gratings (LPG) and Fiber Bragg Gratings (FBG) [3]. In particular, a FBG is an interesting sensor for field instrumentation applications since the measurand is directly inscribed in the reflected Bragg wavelength. The Bragg wavelength is a self-referencing quantity, meaning it is not affected by the source power, connector/splice losses or slow harmonic degradation of the optical link, which would otherwise degrade intensity-modulated measurements [4].

Optical fibre sensors can be classified according to their sensing range as point, quasi-distributed or fully distributed. Quasi-distributed sensing is achieved by writing multiple gratings into a single fibre that each have different Bragg wavelengths, and separating the returns in time or space [5], [6]. This architecture maintains that picometre level wavelength resolution of the individual grating, and reduces the cost of instrumenting large structures by minimizing cabling, conduit, and channel count by putting all these into a single downlead. Thus, it is the configuration used for the structural health monitoring (SHM) of bridges [7], [8] and has been applied as well to geotechnical structures, tunnels and rock masses [9], [10] and, more generally, wherever discrete and well-defined measurement stations are preferred to continuous coverage [13].

The other option is to use fully distributed sensing, using either Raman, Brillouin or Rayleigh backscatter, which provides a profile of the fibre over the whole span, but has been successfully demonstrated for well integrity monitoring [16] and whole-span deformation measurement on railway bridges [17]. Distributed interrogators sacrifice spatial continuity for resolution and acquisition rate; the resolution is normally about an order of magnitude poorer than that of a grating and the spatial resolution is determined by the pulse width, not by the gauge length. If the critical parts of a structure are known in advance, such as mid span sofitter, the bearing zone, a splice or a weld, then a quasi-distributed grating array is still the more economical and more precise instrument.

The channel plan, grating length, apodization profile and interrogation window is best determined by simulation before committing to hardware, since once the fibre is bonded to the structure, the inscription, packaging and installation of a grating array is irreversible. Co-simulation of OptiGrating with OptiSystem has been demonstrated to be capable of reproducing the experimentally measured thermal and mechanical sensitivities of FBG sensors [18] and such an environment has been used to optimise apodized gratings for single-point and quasi-distributed dense WDM sensing networks [19],[20]..

In this context, the present work develops and analyzes OptiSystem models of FBG sensing systems that contribute in the following specific ways:

- The uniform apodized FBG point sensor is modelled and characterised over the temperature range of 30–210 °C, and the elasto-optic sensitivity range of 1–9 με, and the thermal and elasto-optic sensitivity coefficients are determined to calibrate the FBG model.
- A four element quasi-distributed network is built using the calibrated grating and interrogated with WDM at three locations in the sensing network, and the spectral isolation for the channels is verified.
- The simultaneous discrimination of temperature and strain at one point is shown by a pair of gratings placed at the same point, and the demodulation matrix is quoted.
- A representative deployment mapping of the four gratings is created on a three span girder bridge structure, from the simulated channel plan to the required physical instrumentation layout.
- The extracted sensitivities are compared to the numerical and experimental FBG sensing results reported in the time period 2018–2025.

2. Theoretical Background of FBG Sensors

2.1 Structure and Principle of Operation

A fiber Bragg grating is a periodic modulation of the refractive index that is written into the core of a single mode optical fibre, typically created by illuminating a photosensitive germanium doped silica core with an ultraviolet interference pattern formed through an interference mask called a phase mask [3, 4]. The resulting structure is a narrowband, wavelength selective reflector, that reflects a narrow spectral band centered at the Bragg wavelength λ_B and transmits all other spectral components as shown in Fig. 2.

Starting from the first-order phase matching condition between the forward and backward propagating core modes, the Bragg wavelength is found to be:

$$\lambda_B = 2\, n_{eff} \Lambda \qquad (1)$$

where n_{eff} is the effective refractive index of the guided core mode and Λ is the spatial period of the index modulation. Any perturbation that alters either n_{eff} or Λ produces a measurable shift of λ_B , and it is this shift — not the reflected amplitude — that carries the measurement information.

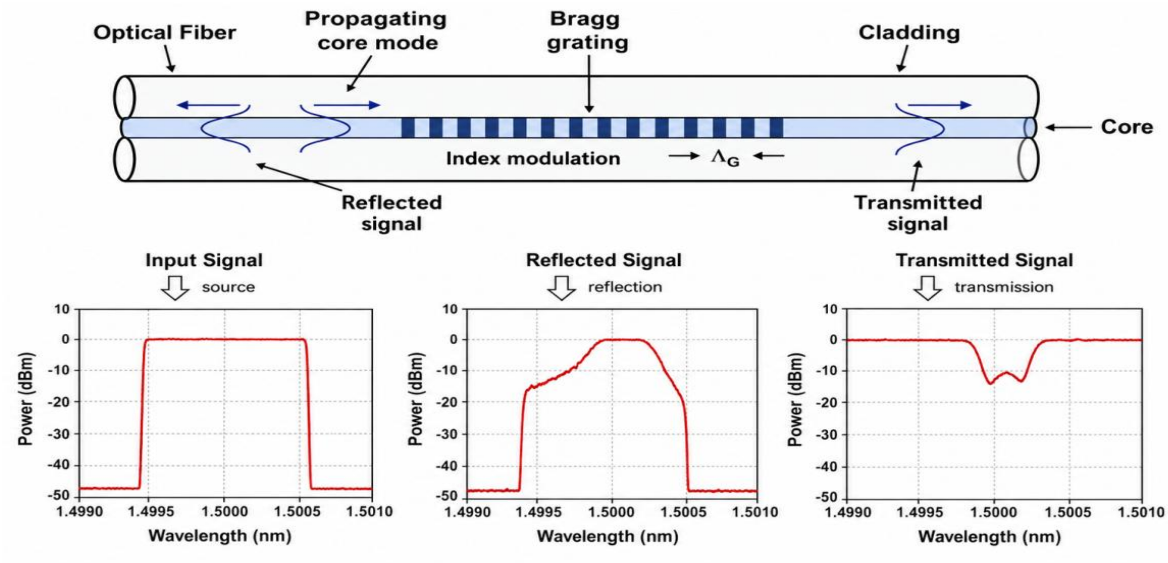

Fig. 2. Schematic of a Fiber Bragg Grating sensor showing the index-modulated core, and the input, reflected and transmitted spectra.

2.2 Temperature Sensitivity

There are two ways that a uniform temperature change ΔT changes the Bragg wavelength: the thermo-optic effect on n_{eff} , and the thermal expansion of Λ. The total first order response is equal to

$$\Delta\lambda_B = \lambda_B(\alpha + \xi)\Delta T \quad (2)$$

where $\alpha \approx 0.55 \times 10^{-6} /°C$ is the thermal expansion coefficient of silica and $\xi \approx 8.6 \times 10^{-6}$ /°C is the thermo-optic coefficient. The thermo-optic term dominates, contributing roughly 94 % of the total response. For a standard single-mode fibre operating near 1550 nm, Eq. (2) predicts a thermal sensitivity of approximately 13–14 pm/°C [21], and experimental characterisations of bare gratings cluster tightly around this figure — for example, 11.48 pm/°C for a 125 µm cladding rising to 11.80 pm/°C after etching to 25 µm [22].

2.3 Strain Sensitivity

If the grating is strained by an axial strain ε, the grating period is increased and at the same time, the strain-optic effect changes the effective index. The net response is

$$\Delta\lambda_B = \lambda_B(1 - p_e)\varepsilon \quad (3)$$

where $p_e \approx 0.22$ is the effective photo-elastic coefficient of silica. At $\lambda_B \approx 1550$ nm this yields approximately 1.2 pm/µε [1]. Because the two responses are of the same physical form, a bonded grating cannot by itself distinguish a mechanical strain from a thermal excursion; the resulting cross-sensitivity is the dominant systematic error in field-deployed FBG strain instrumentation [23].

2.4 Cross-Sensitivity and the Discrimination Matrix

Typically, two gratings are positioned at the same physical location (one fully bonded to the host, one strain-free in a loose tube) and then a linear system is solved to find the two strain sensitivity coefficients. The measured wavelength shifts and unknown measurands are connected by the writing K_T and K_ε of the thermal and mechanical coefficients of each grating.

$$[\Delta\lambda^1, \Delta\lambda^2]^\mathrm{T} = \big[[K_{T1}, K_{\varepsilon 1}], [K_{T2}, K_{\varepsilon 2}]\big] \bullet [\Delta T, \Delta\varepsilon]^\mathrm{T} \quad (4)$$

The system is soluble if the coefficient matrix is well conditioned, that is, when $K_{T1}K_{\varepsilon 2} \neq K_{T2}K_{\varepsilon 1}$. For this reason, the two gratings need to be different in packaging rather than only in wavelength. The matrix approach is used at Location 3 of the quasi-distributed model given in Section IV. Another solution for demodulation is the data driven approach, which is based on neural networks, for the case of multi-grating temperature estimation [24] and for the prediction of the sensitivity of apodized gratings [25].

2.5 Multiplexing Schemes and Channel Planning

This is accomplished through quasi-distributed operation by using a different Bragg wavelength for each grating, and by wavelength division multiplexing (WDM) separation of the returns [26]. The complementary technique is time division multiplexing, which allows for the resolution of gratings with the same wavelength by the round trip delay, and which allows for much longer arrays, at the expense of an interrogator that is pulsed. Hybrid WDM/TDM arrays are possible and femtosecond direct-writing-inscribed serial arrays can be used to create very high number of nodes per array [5].

In a pure WDM array, the channel spacing has to include the width of each grating in addition to the maximum extent of wavelength variations in each grating and a guard-band:

$$\Delta\lambda_{ch} \geq FWHM + |\Delta\lambda_B, max| + \Delta\lambda_{guard} \qquad (5)$$

With a 10 mm apodized grating and a thermal sensitivity of 14.2 pm/°C, a 5 nm channel spacing accommodates an excursion of roughly ±150 °C per node before adjacent channels can begin to interfere. The four-channel plan adopted in Section IV — 1545, 1550, 1555 and 1560 nm — therefore occupies only 15 nm of the C-band and leaves ample headroom within the gain window of a conventional broadband source.

2.6 Apodization and Spectral Quality

100% uniform unapodized grating results in strong side lobes in the reflection spectrum. These side lobes simply increase the noise level of the channel detection algorithm in a single point sensor, while in a densely-packed WDM array they can leak power to adjacent channels, thereby establishing the practical minimum channel spacing. Apodization (grading smoothly to zero at the ends of the grating) has the effect of reducing the amplitude of side lobes at a small sacrifice in reflectivity and the profile determines the trade-off between full width at half maximum, side-lobe suppression ratio and channel isolation [19], [27]. Quasi-distributed optimization of the profiles has been reported to result in the narrower spectral channels and better isolation [28], [29]. In the present models, therefore, there are no apertures or masks in the grating, and the response of the point sensor is the same as the response of the array elements.

3. Point Sensor: Calibration of the Grating Model

3.1 Simulation Setup — Temperature Sensing

In the FBG temperature sensing system, a white-light interrogation scheme was chosen and a high-resolution FBG temperature sensing system was modelled in OptiSystem. The central wavelength of the broadband source is 1500 nm and the power spectral density is −60 dBm/Hz. The grating length of the sensing element is 10 mm and the apodized uniform FBG reduces the noise contribution of the peak estimator, due to the suppression of spectral side lobes in the reflected spectrum, which enhances the accuracy of the wavelength estimation [27].

Ambient temperature was first set at 25 °C and then the sweep was performed from 30 to 210 °C in 20 °C steps. The reflected, transmitted, total signal power, noise power and SNR were measured at each step. The parameter set is complete in Table I, while the layout of the simulation is provided in Fig. 3.

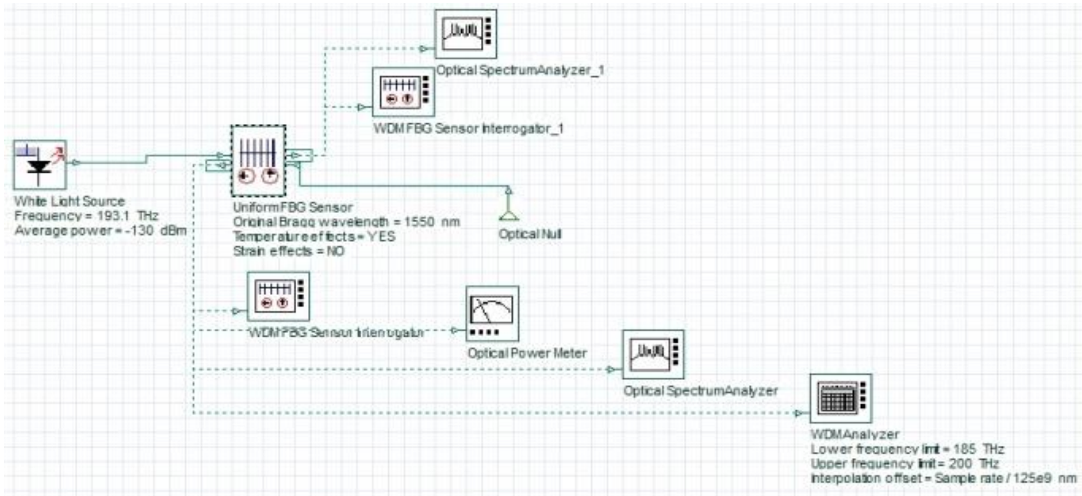

Fig. 3. OptiSystem simulation setup for FBG-based temperature sensing using white-light interrogation.

Table I — Simulation Parameters for the FBG Point Sensor

Parameter	**Value**
Light source type	Broadband white-light
Central wavelength	1500 nm
Power spectral density	−60 dBm/Hz
Grating type	Uniform FBG with apodization
Grating length	10 mm
Temperature sweep range	30 °C to 210 °C (step: 20 °C)
Strain sweep range	1 με to 9 με (step: 2 με)
Initial Bragg wavelength	≈ 1550 nm
Simulation platform	OptiSystem

3.2 Temperature Sensing Results and Discussion

The simulated spectral response is shown in Fig. 4. The reflected spectrum (Fig. 4(a)) has a well-defined single-peak profile with a 3 dB bandwidth of 10 mm, which corresponds to the grating's length; the transmitted spectrum (Fig. 4(b)) shows a corresponding notch, confirming that energy was conserved across the grating. With an increase in temperature, the reflected peak position monotonically moves towards longer wavelength, consistent with the thermo-optic and thermal expansion mechanisms of Eq. (2).

The Bragg wavelength versus temperature characteristic (Fig. 4(c)) is linear over all the sweep. When the 10 values listed in Table II are plotted on a graph and a best fit is applied using least squares program, the slope of the curve is 14.2 pm/°C and the spread of the values is less than 0.01 nm. For the Bragg wavelength of around 1550 nm, this value is in good agreement with those reported for conventional germanosilicate fibre [21, 22], and is the value predicted by Eq. (2) for $\alpha + \xi = 9.15 \times 10^{-6}$ /°C. The total signal power (Fig. 4(d)) is held to within a narrow range of

±0.8 dBm, showing the reflectivity of the apodized grating to be essentially the same across the swept range. At the highest temperatures, the maximum SNR (Fig. 4(e)) oscillates about 35 dB, and the minimum SNR (Fig. 4(f)) starts to drop with increasing temperature due to the increased wideband thermal noise [18]. As the temperature moves from 30 °C to above 150 °C, the tabulated noise power in Table II decreases from 27.52 dBm to below 10 dBm and the minimum SNR recovers from strongly negative values to positive values; this confirms that it is the relative weight of the noise floor with respect to the reflected peak, rather than the peak itself, that determines the demodulation margin.

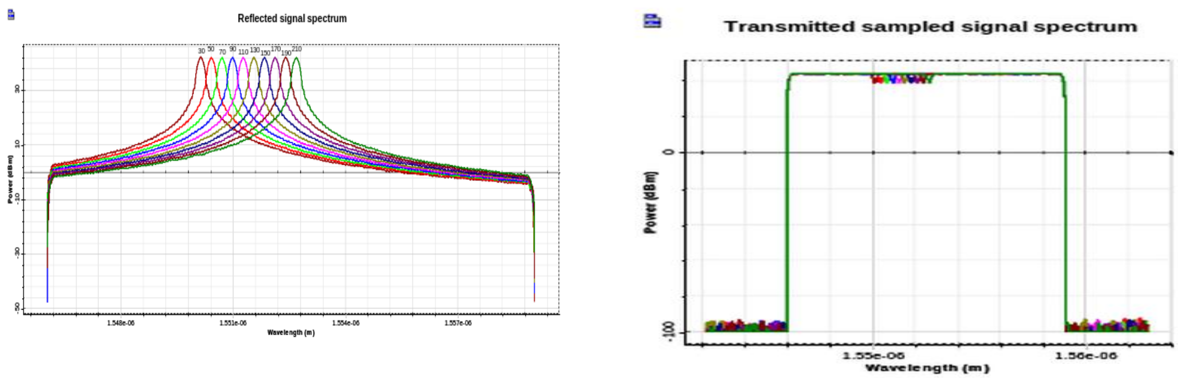

(a) Reflected signal spectrum. (b) Transmitted signal spectrum.

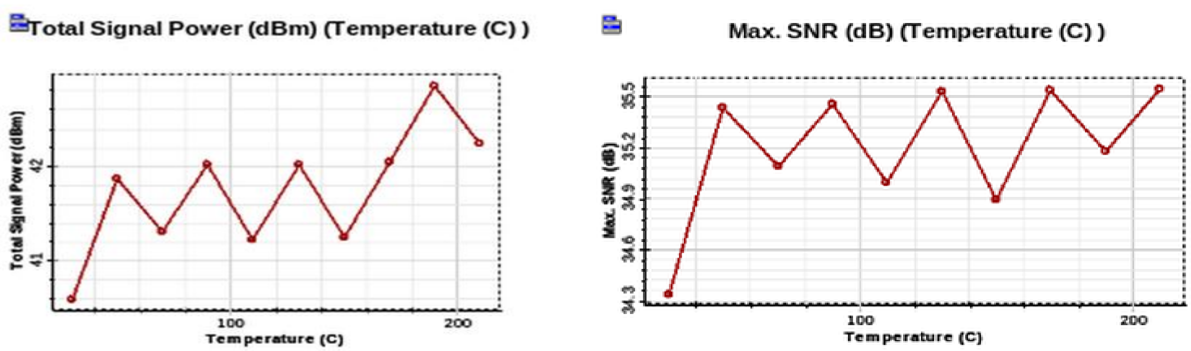

(c) Temperature vs. Bragg wavelength (nm). (d) Temperature vs. total signal power (dBm).

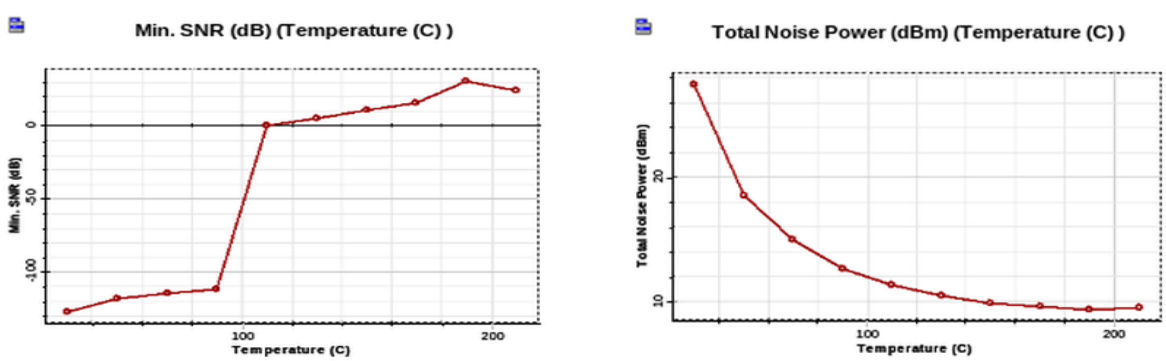

(e) Temperature vs. maximum SNR (dB). (f) Temperature vs. minimum SNR (dB).

Fig. 4. Simulated spectral results of the FBG temperature point sensor.

Table II — FBG Spectral Characteristics Versus Temperature

Temp. (°C)	Bragg λ (nm)	Signal Power (dBm)	Noise Power (dBm)	Max. SNR (dB)	Min. SNR (dB)
30	1550.14	40.59	27.52	34.33	−127.49
50	1550.43	41.87	18.52	35.44	−118.25
70	1550.71	41.32	14.96	35.09	−114.33
90	1550.99	42.02	12.67	35.45	−111.45
110	1551.28	41.22	11.30	34.99	0.39
130	1551.56	42.02	10.43	35.53	5.44
150	1551.84	41.25	9.86	34.89	10.64
170	1552.13	42.04	9.61	35.54	15.79
190	1552.41	42.86	9.33	35.17	30.85
210	1552.69	42.25	9.53	35.55	23.99

3.3 Simulation Setup — Strain Sensing

The strain sensing model is based on the same broadband source and grating setup, but the thermal load is fixed while a controlled axial strain is applied in steps of 2 με, ranging from 1 με to 9 με. All of the following parameters: reflected spectrum, transmitted spectrum, Bragg wavelength, signal power and noise power and SNR are monitored simultaneously using dedicated optical display units as illustrated in Fig. 5.

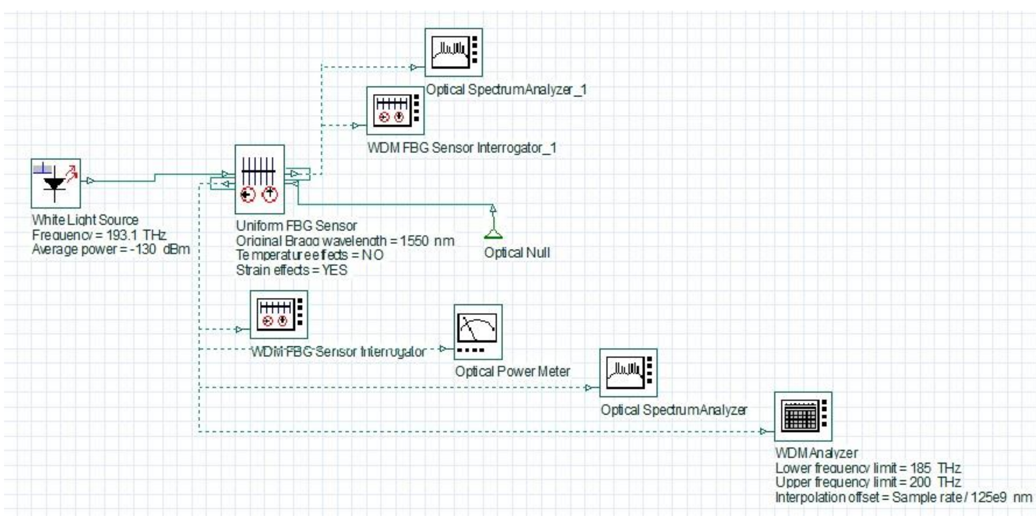

Fig. 5. OptiSystem simulation setup for FBG-based strain sensing with multi-output monitoring.

3.4 Strain Sensing Results and Discussion

The results of the strains simulated are shown in Fig. 6. The reflected spectrum (Fig. 6(a)) and transmitted spectrum (Fig. 6(b)) demonstrate the theoretically expected shift of the spectra with increasing load, and Fig. 6(c) illustrates the linear relationship expected from Eq. (3) between Bragg wavelength and strain. The extracted strain sensitivity is around 1.2 pm/με, which is nearly the same as the theoretical value for germanosilicate fibre and reported values on bare gratings [1], [22].

The total signal power (shown in Fig. 6(g)) and noise power (shown in Fig. 6(d)) are not uniform throughout the strain range, and the SNR characteristics are shown in Figs. 6(e) and 6(f) are still good for reliable demodulation. The plots of wavelength tracking (Figs. When the residual side-lobe structure of the apodized grating is comparable to the main lobe at the ends of the sweep, as in 6(h) and 6(i), the peak estimator separates the Bragg wavelength at two dominant spectral positions. The results of the extensive strains are presented in Table III. It should be noted that the total wavelength excursion predicted by Eq. (3) over the 1-9 με span is approximately 10 pm, with a comparable resolution of the modeled interrogator, and so the sweep does not resolve individual microstrain increments but only serves to validate the linear relationship and the sign of the elasto-optic response; the SNR entries in Table III are therefore dominated by the noise floor.

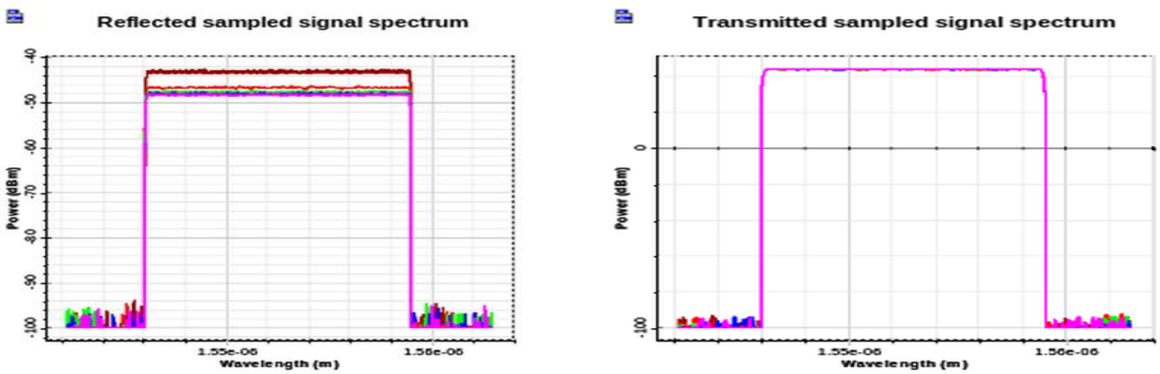

(a) Reflected signal spectrum. (b) Transmitted signal spectrum.

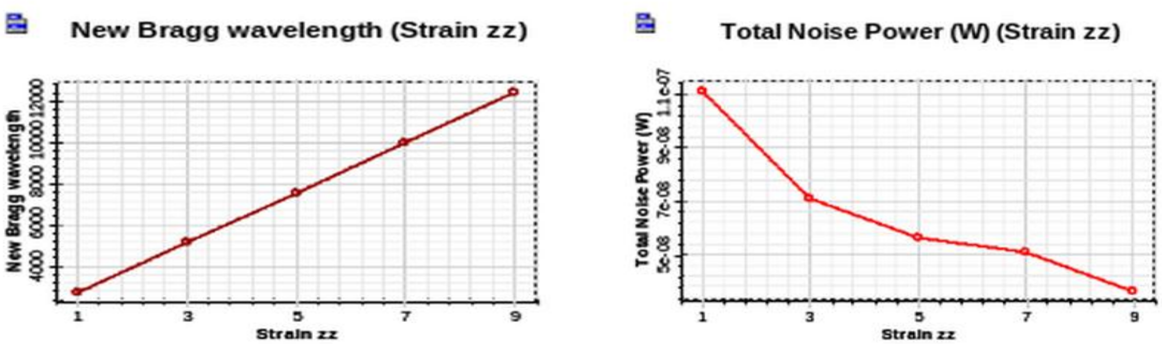

(c) Strain vs. Bragg wavelength (nm). (d) Strain vs. total noise power (W).

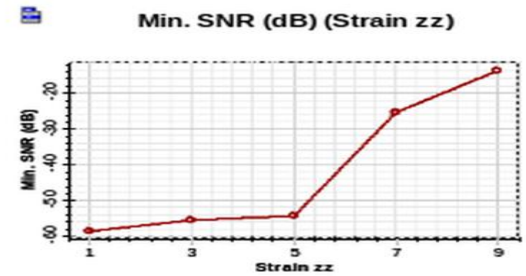

(e) Strain vs. maximum SNR (dB). (f) Strain vs. minimum SNR (dB).

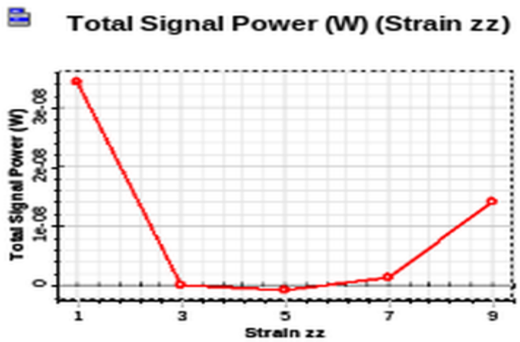

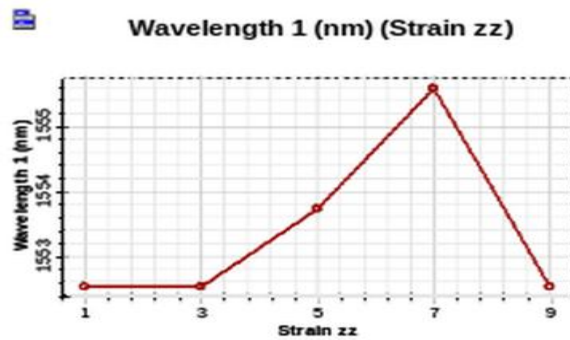

(g) Strain vs. total signal power (W). (h) Strain vs. wavelength 1 (nm).

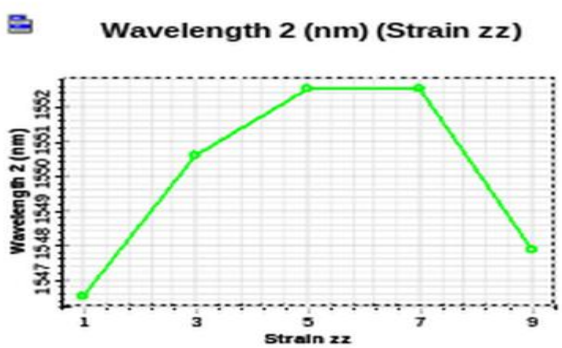

(i) Strain vs. wavelength 2 (nm).

Fig. 6. Simulated spectral results of the FBG strain point sensor.

Table III — FBG Spectral Characteristics Versus Axial Strain

Strain (με)	Max. SNR (dB)	Min. SNR (dB)	Signal-power peak wavelength* (nm)	Noise-power peak wavelength* (nm)
1	−0.08	−58.73	1546.52	1552.52
3	−9.81	−55.71	1550.60	1552.52

5	−54.50	−54.51	1552.52	1553.73
7	−13.22	−25.49	1552.52	1555.59
9	0.47	−13.79	1547.88	1552.52

** Peak wavelength positions corresponding to the maximum signal power and noise power channels (nm).*

4. Quasi-Distributed FBG Sensor System

4.1 Background and Motivation

A quasi-distributed scheme multiplexes several gratings onto the same fibre, uses a different Bragg wavelength for each one and discriminates between returns using WDM interrogation. One fibre strand and one interrogator then check the physical parameters at stations separated by space [30]. The cost of routing and protecting and terminating conventional instrumentation cable is overwhelming the sensor cost in large-scale monitoring such as pipeline integrity, bridge assessment, geotechnical monitoring, and the monitoring of concrete structures under thermal load [31].

4.2 Simulation Setup

A quasi-distributed system was realised in OptiSystem with a broadband source of 193.1 THz at an average power of −130 dBm. Four uniform apodized (10 mm) FBGs were placed at three sensing points along the fibre, with optical delay elements placed between the sensing groups to ensure sufficient spatial separation between the returns. The reflected channels are isolated by using an optical circulator and are analysed by a WDM interrogator, optical spectrum analyzer, optical power meter and a peak detector; the transmitted spectrum is monitored separately at the far end of the array. The architecture is sketched in Fig. 7.

Four centre wavelengths were set as follows: FBG-1 at 1545 nm (Location 1, temperature), FBG-2 at 1550 nm (Location 2, temperature), FBG-3 at 1555 nm (Location 3, temperature) and FBG-4 at 1560 nm (Location 3, strain). The co-located grating pair is therefore employed at location 3, and allows the simultaneous temperature–strain discrimination as described by Eq. (4). The uniform channel spacing of 5 nm meets the guard-band condition of Eq. (5) with a large margin. The configuration is summarised in Table IV.

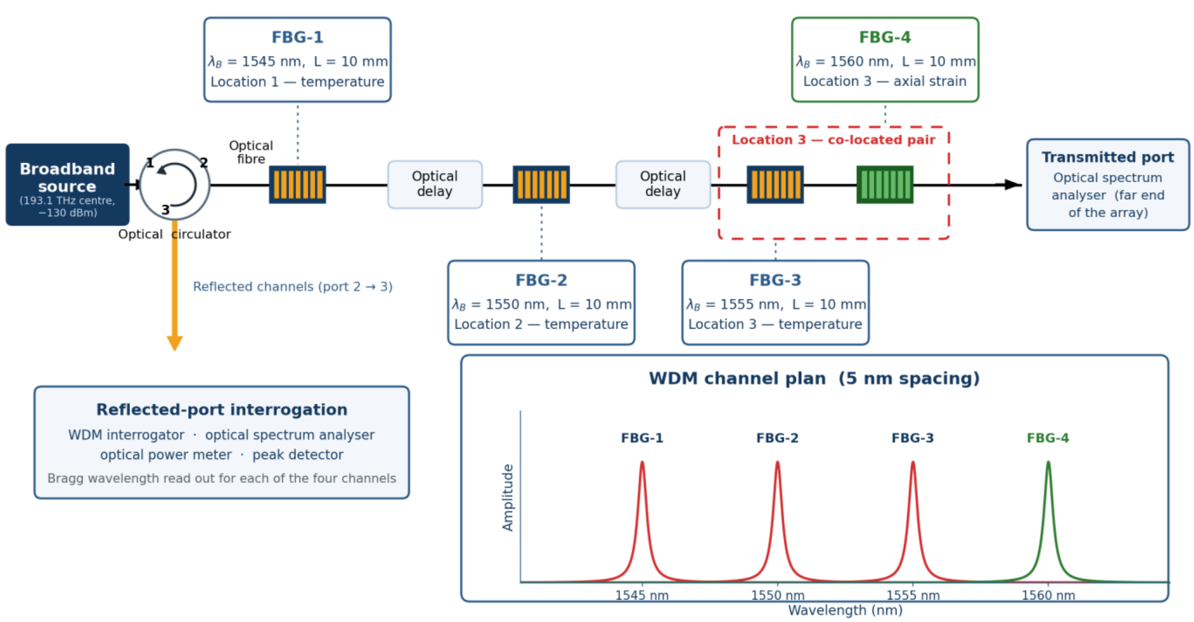

Fig. 7. Architecture of the simulated quasi-distributed FBG sensor system: four gratings at three sensing locations on a single fibre, interrogated by WDM through an optical circulator. FBG-3 and FBG-4 form the co-located pair at Location 3. Reflected channels return through port 3 of the circulator to the WDM interrogator, optical spectrum analyser, optical power meter and peak detector, while the transmitted spectrum is monitored at the far end of the array. The inset shows the four-channel WDM plan at 5 nm spacing.

Table IV — Quasi-Distributed FBG Sensor Configuration

FBG No.	Centre λ (nm)	Sensing Location	Measurand	Grating Length
1	1545	Location 1	Temperature	10 mm
2	1550	Location 2	Temperature	10 mm
3	1555	Location 3	Temperature	10 mm
4	1560	Location 3	Axial strain	10 mm

4.3 Simulation Results and Discussion

The simulated responses of the quasi-distributed system are displayed in Fig. 8. The transmitted spectrum (Fig. 8(a)) has four distinct notches at 1545, 1550, 1555 and 1560 nm, which is the result of complete spectral isolation and successful WDM multiplexing, while the reflected spectrum (Fig. 8(c)) has four well-resolved peaks. Both the two-dimensional and the three-dimensional spectral representations (Figs. For signal fidelity, 8(b) and 8(d) show that the fidelity of the signal is preserved in all channels, while there is no measurable power transfer between neighbouring channels at the spacing of 5 nm.

The Bragg wavelength value of FBG-1 changes in a linear manner with temperature at Location 1 (Figs. 8(e) and 8(f)) that are sensitive as per the calibrated point sensor. It is observed that the thermal response is essentially the same for Location 2 (Figs. 8(g) and 8(h) show uniform values for the independently interrogated nodes. FBG-3 exhibits a linear relationship between temperature at Location 3 (Figs. 8(i) and 8(j) are the result of applied axial load on FBG-4 while the FBG-5 responds independently (Figs. The feasibility of simultaneous multiple parameter discrimination by spectrally isolated gratings at a single physical station is illustrated by 8(k) and 8(l)).

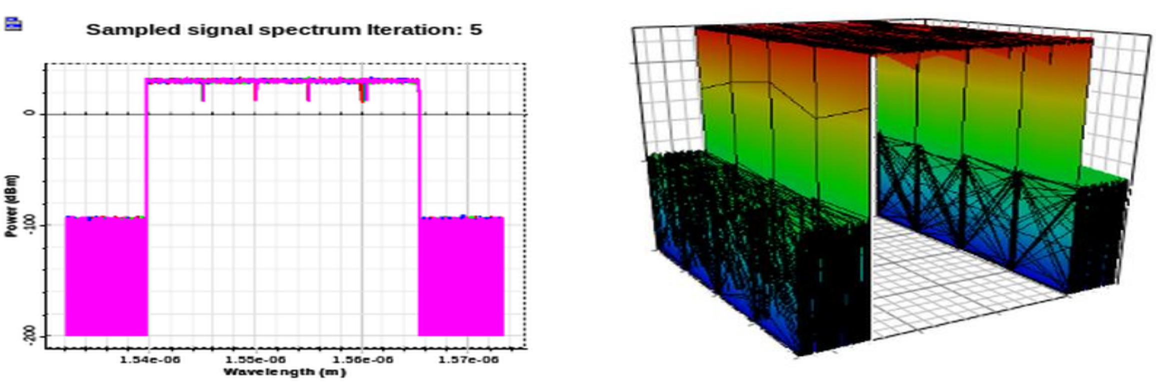

(a) Transmitted spectrum. (b) 3D transmitted spectrum.

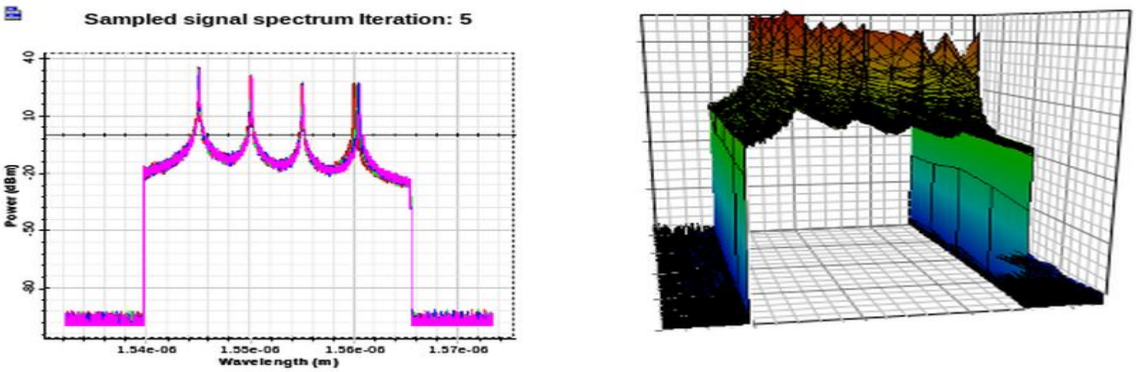

(c) Reflected spectrum. (d) 3D reflected spectrum.

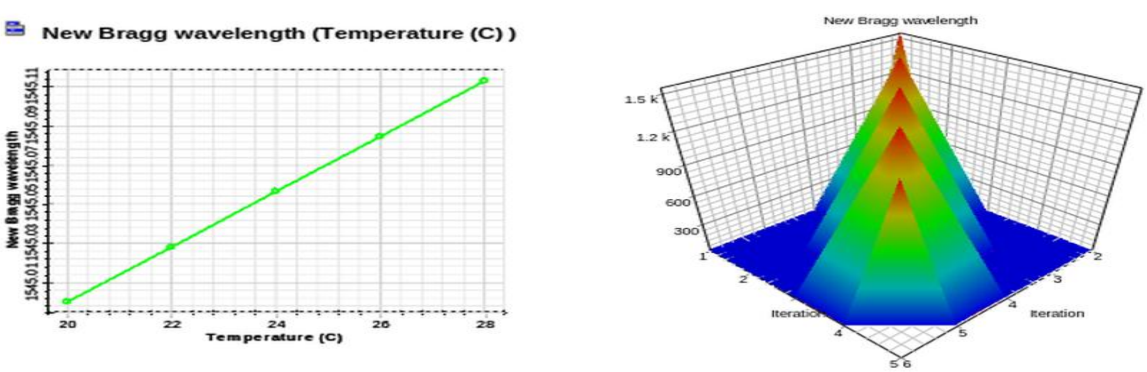

(e) Temperature vs. wavelength — Location 1 (2D). (f) Temperature vs. wavelength — Location 1 (3D).

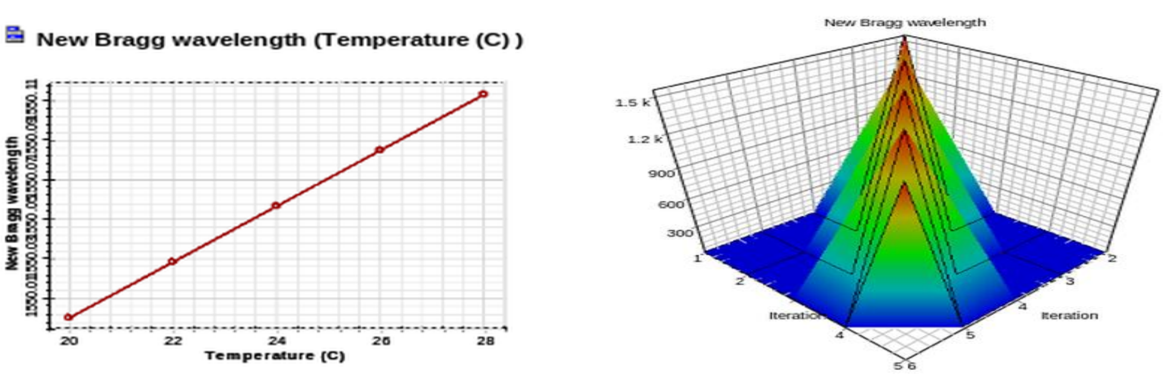

(g) Temperature vs. wavelength — Location 2 (2D). (h) Temperature vs. wavelength — Location 2 (3D).

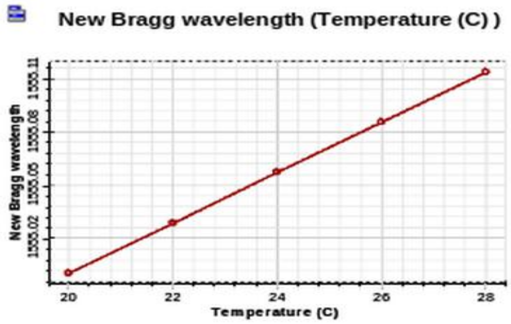

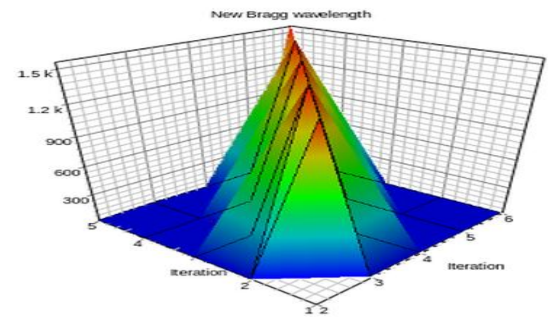

(i) Temperature vs. wavelength — Location 3, FBG-3 (2D). (j) Temperature vs. wavelength — Location 3, FBG-3 (3D).

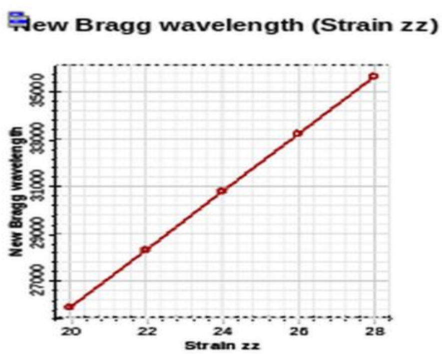

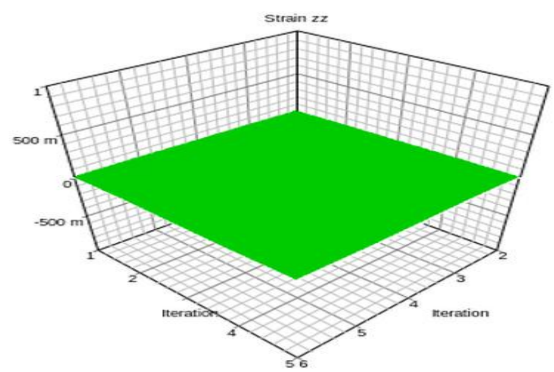

(k) Strain vs. wavelength — Location 3, FBG-4 (2D). (l) Strain vs. wavelength — Location 3, FBG-4 (3D).

Fig. 8. Simulated responses of the quasi-distributed FBG sensor system.

Table V — Bragg Wavelength Versus Temperature at All Sensing Locations

Temperature (°C)	Location 1 λ_B (nm)	Location 2 λ_B (nm)	Location 3 — FBG-4 λ_B (nm)
20	1545.00	1550.00	1560.00
22	1545.03	1550.03	1560.15
24	1545.06	1550.06	1560.30
26	1545.08	1550.09	1560.45
28	1545.11	1550.11	1560.60

The sensitivity coefficients have been obtained from these data by linear regression and are summarised in table VI. Nodes 1 and 2 both return 13.8 pm/°C. The offset relative to the 14.2 pm/°C measured by the point sensor is not a physical difference, but rather a quantisation artefact: The difference between the two numbers is within about ±1.25 pm/°C, which is the smallest significant digit in the tabulated values over the 8 °C range.

Note that the third column in Table V needs to be interpreted with care. FBG-4 is the channel listed for Location 3, and is the strain-sensing grating of this co-located pair; it is the one being strained during this sweep. Therefore, its apparent coefficient is not a thermal sensitivity, but a thermo-mechanical response, and its discrimination matrix, shown in Eq. (4), is able to separate the two contributions, with the strain-free reference FBG-3 being measured at the wavelength of 1555 nm. The ratio of the apparent coefficient at Location 3 to the true thermal coefficient at Locations 1 and 2 gives a direct measure of the mechanical contribution and hence of the conditioning of the matrix.

Table VI — Sensitivity Coefficients Extracted from the Quasi-Distributed Model

Sensing node	Grating	Centre λ (nm)	Δλ over sweep (nm)	Extracted coefficient	Interpretation
Location 1	FBG-1	1545	0.11 / 8 °C	13.8 pm/°C	Thermal only
Location 2	FBG-2	1550	0.11 / 8 °C	13.8 pm/°C	Thermal only
Location 3	FBG-3	1555	—	≈ 13.8 pm/°C	Thermal reference
Location 3	FBG-4	1560	0.60 / 8 °C	75 pm/°C (apparent)	Combined thermal + mechanical
Point sensor	Reference	1550	2.55 / 180 °C	14.2 pm/°C	Calibration baseline

Coefficients obtained by linear regression on the tabulated data. The apparent coefficient of FBG-4 includes the mechanical contribution of the applied axial load and is resolved by the discrimination matrix of Eq. (4).

4.4 Representative Deployment: Instrumentation of a Girder Bridge

The four-grating array is then simulated on a typical 3-span reinforced concrete girder bridge (Fig. 9) to illustrate the translation from the simulated channel plan to a physical installation. The quasi-distributed grating arrays are typically specified for this type of structure, because the sections of interest (mid-span soffits and bearing zones) are few in number and can be known from the design analysis [7], [8].

A single downlead provides access to the entire array from an interrogator cabinet at abutment A1. The sensing fibre is housed in a protective conduit attached to the girder soffit, so that the optical cable only crosses the structure once and one optical connector is left exposed at the cabinet. FBG-1 is placed at the mid-span soffit of span 1, FBG-2 is placed in the bearing zone over pier P1, and the two FBG's (FBG-3 and FBG-4) are co-located at the mid-span soffit of span 2, where the sagging moment of the span is at a maximum and therefore the mid-span soffit would be the critical location for the strain caused by live-loads. All the gratings and how they are installed are listed in Table VII.

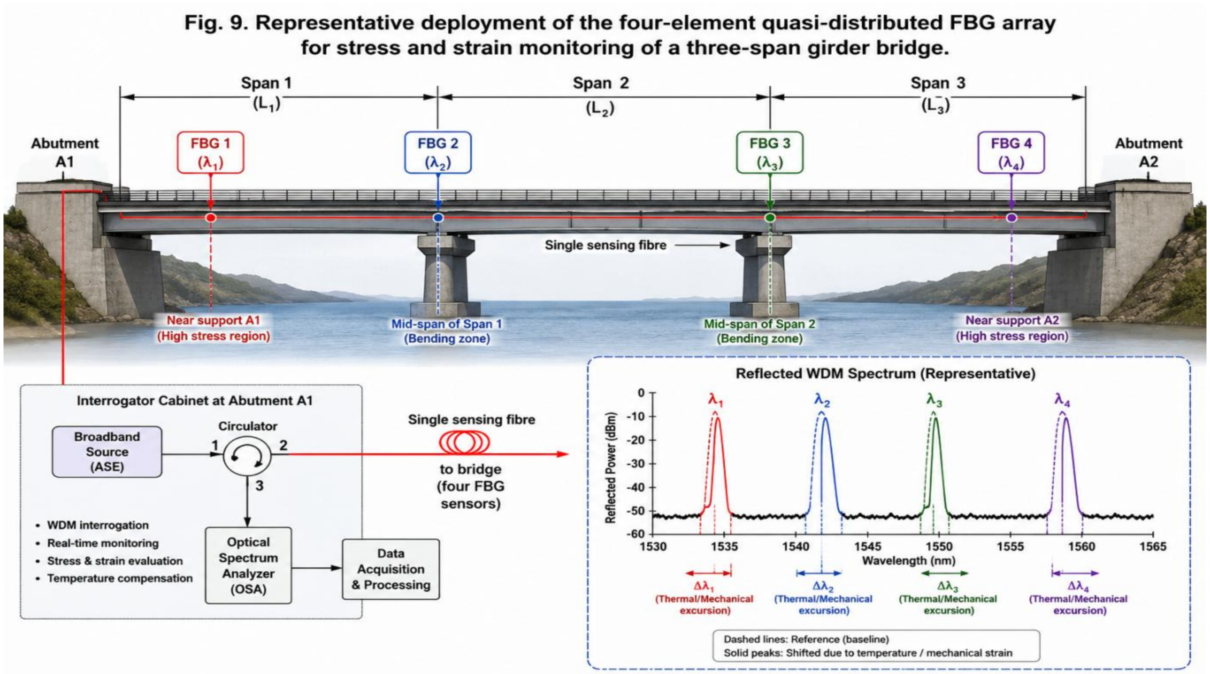

Fig. 9. Representative deployment of the four-element quasi-distributed FBG array for stress and strain monitoring of a three-span girder bridge. A single sensing fibre carries all four wavelength channels from the interrogator cabinet at abutment A1; the inset shows the reflected WDM spectrum with the thermal and mechanical wavelength excursions indicated.

Table VII — Mapping of the Simulated Channel Plan onto the Bridge Instrumentation Layout

FBG	λ_B (nm)	Structural element	Measurand	Monitoring purpose	Installation method
FBG-1	1545	Span-1 girder soffit, mid-span	Temperature	Thermal state of the approach span; input to thermal correction of span-1 data	Loose tube, strain-isolated
FBG-2	1550	Bearing zone above pier P1	Temperature	Thermal expansion at the bearing and expansion joint	Loose tube, strain-isolated
FBG-3	1555	Span-2 girder soffit, mid-span	Temperature	Strain-free thermal reference for FBG-4	Loose tube within 100 mm of FBG-4
FBG-4	1560	Span-2 girder soffit, mid-span	Axial strain	Live-load flexural strain, long-term deflection trend, crack onset	Fully bonded to the prepared concrete surface with structural epoxy

From the simulation results, there are three practical considerations that follow. The first is that the pairing of FBG-3 and FBG-4 is not optional: The form of Eq. (2) and Eq. (3) are the same, so the bonded-only FBG installed on the bridge soffit cannot distinguish the 10 °C diurnal temperature swing (about 144 pm) from a mechanical strain of approximately 120 με. The second equation needed by Eq. (4) is provided by the strain-free companion grating, which is required to be physically adjacent to the first grating, so that both gratings experience the same thermal field.

Secondly, the loss budget is dominated by installation, not by the gratings. When added together, the four channels will occupy a total of 15 nm of spectrum, and the reflectivity of each apodized grating is fairly low, so the array will have relatively small insertion loss - limited only by the splice loss on the cabinet and the bend radius of the conduit at the pier crossings. These losses do not affect the calibration, but only the SNR margin, which is the main practical benefit of the FBG over intensity-modulated instrumentation as the measurand is wavelength-encoded.

Third, the packaging that surrounds the test kit is the third factor responsible for the laboratory sensitivity remaining in the field. The value of the strain transfer coefficient of coated and encapsulated gratings differs from the bare fibre value and the coating material and the bonding process must be characterised if the extracted 1.2 pm/με is to be used for field data [23], [32]. However, if the quantity of interest is the displacement, then packages for mechanical transducing of the grating have been developed to provide an amplified axial strain in response to the deflection [33].

5. Comparison with Recently Reported Work

The coefficients obtained in Sections III and IV are compared with the numerical and experimental results available in the literature for FBG temperature and strain sensors from 2018 to 2025 in Table VIII. Only the studies that simulate or measure the wavelength response of a silica FBG under temperature and/or axial load are considered in the comparison for the sensitivity figures to be directly comparable.

Table VIII — Comparison of the Present Results with Recently Reported FBG Sensing Studies

Study	Method / platform	Configuration	Thermal sensitivity (pm/°C)	Strain sensitivity (pm/με)	Principal observation
Elgaud et al. [18] (2016)	OptiGrating + OptiSystem co-simulation	Two Gaussian-apodized gratings, remote point sensing	14.4	1.2	Reference co-simulation demonstrating strain-independent temperature readout
Mohammed & El Serafy [27] (2018)	Coupled-mode theory, numerical optimisation	Quasi-distributed apodized array	—	—	Apodization profile optimised for FWHM and side-lobe suppression
Kumar et al. [22] (2021)	Experiment, etched / un-etched grating pair	Dual point gratings, simultaneous readout	11.48 – 11.80	1.06 – 1.20	Sensitivity rises as cladding is etched from 125 µm to 25 µm

Zhong et al. [5] (2022)	Experiment, femtosecond direct writing	Series-integrated grating array	—	—	High-density quasi-distributed arrays with fine spatial resolution
Qin et al. [23] (2023)	Experiment, substrate-embedded gratings	Point sensor on several substrates	—	—	Quantifies strain–temperature cross-sensitivity versus substrate and preload
Mandal & Sidhishwari [20] (2024)	Numerical, proposed apodization profile	Four-FBG WDM network, 2 nm spacing	—	—	Detectable ranges of 153 °C and 1439 με reported for the optimised profile
Sanipatin et al. [34] (2024)	Experiment, tapered FBG in PDMS with microsphere	Sensitised point sensor	47.19 – 221.2	—	Large thermal gain from the polymer, at the cost of a fragile, non-standard package
This work	OptiSystem, apodized uniform FBG	Point calibration plus four-FBG WDM quasi-distributed array, 5 nm spacing	14.2 (point); 13.8 (array)	≈ 1.2	Full spectral isolation of four channels with temperature–strain discrimination at one node

A dash indicates that the quantity was not the reported figure of merit of that study; those works optimise spectral quality, packaging or array density rather than the wavelength sensitivity itself.

Three observations follow. First, the thermal and mechanical coefficients found here are in the range of both simulation and experimental measurements done on bare gratings close to 1550 nm. The agreement between the co-simulation of Elgaud et al. is exact as both models use the same thermo-optic and elasto-optic constants, whereas the experimental values of Kumar et al. are about 15–20 % lower – a systematic difference that is likely due to finite strain and heat transfer from a physically mounted fibre, not reproduced by an idealised model.

Secondly the studies that claim much higher sensitivity modify the transducer, not the grating. The Sanipatin et al. device is tapered and encapsulated in PDMS, with the polymer increasing the thermal expansion that the fibre sees, to 221.2 pm/°C, which is an order of magnitude greater than the bare-fibre. The gains are real, but at the cost of a reduced measurement range, additional hysteresis, and a package that is hard to multiplex in long serial arrays — the very cost/benefit that makes the unmodified grating appealing for the multi-node bridge application discussed here.

Thirdly, the quasi-distributed studies all share the same design variable—spectral isolation. The present model uses a spacing of 5 nm, while Mandal and Sidhishwari use an optimised apodization profile to get four grating spacing at 2 nm. There are fewer side lobes available with a similar plan, but there is a greater requirement for control of the side-lobe structure, and less headroom for the wavelength excursion of each node. The tighter plan should be used with a narrow ambient range while the conservative spacing is the more safe engineering solution with a wide ambient range.

6. Discussion and Limitations

The following idealisations of the simulation environment were formulated explicitly as it puts limitations on the extent to which the coefficients extracted from the simulation can be transferred to a field installation.

- The strain sweep covers a range of 10 pm (approximately 10 resolution elements of the interrogator modeled) over a wavelength excursion of 1–9 sweeps. It verifies the linearity and sign of the elasto-optic effect, but does not apply the sensor over a range of strains typically experienced on a real bridge, which are in the range of 50–200 με. The following is a plot of the results of equation (3) outside this range, which may be extrapolated well beyond, but for which, however, experimental confirmation at realistic loads is needed.
- Strain transfer is considered to be 100%. In practice, the combined effect of the adhesive layer, coating and surface preparation will determine the percentage of the host strain that will reach the grating, thus giving the bonded package a different effective sensitivity than the bare-fibre value [32].
- It is assumed that there is no variation in the thermal field across the 10 mm gauge. A high value of the gradient over the grating will widen and smear the reflected peak instead of shifting the peak, and thus bias any peak tracking estimator.
- A long-term drift mechanism is not included in the model. Grating decay, coating relaxation and adhesive creep is a process that takes months or years and cannot be determined in a spectral simulation; long-term stability has to be determined by experiment.
- The interrogation is idealised. The SNR values in Tables II and III are based on the modelled noise sources and a field interrogator introduces its own wavelength reference drift.

These restrictions suggest the natural extensions of this work. The discrete grating array and continuous backscatter profile could then be compared against a field validator that is distributed. On the demodulation side, machine-learning estimators are also used on grating arrays as well as Brillouin distributed systems, and provide a path to solving the multi-parameter cross-sensitivity without an explicitly inverted coefficient matrix [24], [35]. Finally, the model of the sensor can be extended to apply to microstructured and specialty fibres, enabling the extra recovery of other measurands from a single sensor node [36].

7. Conclusion

This paper has reported a systematic simulation study of Fiber Bragg Grating sensors for temperature measurement and axial strain measurement, starting from a single-grating calibration model, to the four-element quasi-distributed sensor network, and finally to a representative bridge instrumentation model. The main results are summarized below.

(1). The apodized uniform FBG point sensor has a linear Bragg wavelength shift of 14.2 pm/°C over the temperature range of 30-210 °C. The signal power is maintained within ±0.8 dBm and the maximum SNR is maintained at roughly 35 dB throughout the entire operating temperature range, with the minimum SNR getting better with increasing temperature due to the ever-decreasing noise floor.

(2). The grating shows the linear variation of the wavelength, consistent with the elasto-optic model, between 1 and 9 με of axial loading. Both coefficients agree with known experimental values of bare germanosilicate fibre.

(3). The quasi-distributed system of four WDM-multiplexed gratings at 1545, 1550, 1555 and 1560 nm achieves complete spectral isolation between channels at 5 nm spacing, a stable linear temperature response at all three sensing nodes, and simultaneous temperature–strain discrimination at Location 3 through a co-located grating pair. The point-sensor calibration and the regression on the multiplexed data give 13.8 pm/°C at the temperature nodes, with excellent agreement to within the quantisation of the tabulated wavelengths.

(4). The channel plan is directly applicable to a physical instrumentation layout for a three-span girder bridge - a single downlead is used for four sensing channels at the mid-span soffits and the bearing zone and the strain grating is paired with a strain-free thermal reference at the critical section.

(5). Comparing the extracted coefficients to studies conducted in the time period 2018 to 2025 puts the extracted coefficients in the range that is established for bare gratings, and helps explain the balancing act between sensitised packages, which can have much larger coefficients, but at the expense of range and multiplexability, and unmodified gratings, which are the best option for dense serial arrays.

In total, the results presented here provide a validated simulation tool that can be used as a design tool for FBG based sensing networks in structural health monitoring, industrial process control, aerospace and geophysical applications. Future work will focus on advanced apodization profiles for tighter channel plans, experimental validation of the strain response at realistic loads, cross-sensitivity compensation with data-driven demodulation and extension to hybrid architectures of quasi-distributed and fully-distributed architectures.

Conflict of Interest

The authors declare no conflict of interest regarding the publication of this paper.

REFERENCES

1. C. E. Campanella, A. Cuccovillo, C. Campanella, A. Yurt, and V. M. N. Passaro, "Fibre Bragg grating based strain sensors: Review of technology and applications," Sensors, vol. 18, no. 9, art. 3115, Sep. 2018, doi: 10.3390/s18093115.
2. J. K. Sahota, N. Gupta, and D. Dhawan, "Fiber Bragg grating sensors for monitoring of physical parameters: A comprehensive review," Opt. Eng., vol. 59, no. 6, art. 060901, Jun. 2020, doi: 10.1117/1.OE.59.6.060901.
3. A. Theodosiou, "Recent advances in fiber Bragg grating sensing," Sensors, vol. 24, no. 2, art. 532, Jan. 2024, doi: 10.3390/s24020532.
4. T. Erdogan, "Fiber grating spectra," J. Lightw. Technol., vol. 15, no. 8, pp. 1277–1294, Aug. 1997, doi: 10.1109/50.618322.
5. H. Zhong et al., "Quasi-distributed temperature and strain sensors based on series-integrated fiber Bragg gratings," Nanomaterials, vol. 12, no. 9, art. 1540, May 2022, doi: 10.3390/nano12091540.
6. K. Kuroda, "Long-distance quasi-distributed FBG sensor system based on time-division multiplexing," IEEE Photon. Technol. Lett., vol. 36, no. 18, pp. 1133–1136, Sep. 2024, doi: 10.1109/LPT.2024.3447012.
7. Z. Deng, M. Huang, N. Wan, and J. Zhang, "The current development of structural health monitoring for bridges: A review," Buildings, vol. 13, no. 6, art. 1360, May 2023, doi: 10.3390/buildings13061360.
8. Z. He, W. Li, H. Salehi, H. Zhang, H. Zhou, and P. Jiao, "Integrated structural health monitoring in bridge engineering," Autom. Constr., vol. 136, art. 104168, Apr. 2022, doi: 10.1016/j.autcon.2022.104168.
9. M. J. Singh and S. Choudhary, "Applications of fibre Bragg grating sensors for monitoring geotechnical structures: A comprehensive review," Measurement, vol. 218, art. 113171, Aug. 2023, doi: 10.1016/j.measurement.2023.113171.
10. M. Liang, X. Fang, Y. Song, S. Li, N. Chen, and F. Zhang, "Research on three-dimensional stress monitoring method of surrounding rock based on FBG sensing technology," Sensors, vol. 22, no. 7, art. 2624, Mar. 2022, doi: 10.3390/s22072624.
11. M. Mishra, P. B. Lourenço, and G. V. Ramana, "Structural health monitoring of civil engineering structures by using the Internet of Things: A review," J. Building Eng., vol. 48, art. 103954, May 2022, doi: 10.1016/j.jobe.2021.103954.
12. C. Cui, L. Gao, and N. Dai, "Fiber Bragg grating inclinometer-enabled IoT sensing system with low power consumption and small size," Sens. Mater., vol. 33, no. 7, pp. 2321–2331, 2021, doi: 10.18494/SAM.2021.3281.
13. S. Hassani and U. Dackermann, "A systematic review of advanced sensor technologies for non-destructive testing and structural health monitoring," Sensors, vol. 23, no. 4, art. 2204, Feb. 2023, doi: 10.3390/s23042204.

14. P. Lu et al., "Distributed optical fiber sensing: Review and perspective," Appl. Phys. Rev., vol. 6, no. 4, art. 041302, Dec. 2019, doi: 10.1063/1.5113955.
15. Y. Du and C. Ye, "Rayleigh scattering-based single mode–graded index multimode–coreless fiber structure for distributed liquid detection," Opt. Express, vol. 31, no. 22, pp. 35948–35959, Oct. 2023, doi: 10.1364/OE.506039.
16. R. Amer, Z. Xue, T. Hashimoto, and T. Nagata, "Distributed fiber optic temperature and strain sensing in cementing and water injection: Insights to well integrity monitoring and multisensing optical fiber cable design," Gas Sci. Eng., vol. 130, art. 205430, Oct. 2024, doi: 10.1016/j.jgsce.2024.205430.
17. K. Kishida, T. L. Aung, and R. Lin, "Monitoring a railway bridge with distributed fiber optic sensing using specially installed fibers," Sensors, vol. 25, no. 1, art. 98, Dec. 2024, doi: 10.3390/s25010098.
18. M. M. Elgaud, M. S. D. Zan, A. A. G. Abushagur, and A. A. A. Bakar, "Analysis of independent strain–temperature fiber Bragg grating sensing technique using OptiSystem and OptiGrating," in Proc. IEEE 6th Int. Conf. Photon. (ICP), Kuching, Malaysia, Mar. 2016, pp. 5–7, doi: 10.1109/ICP.2016.7510036.
19. N. A. Mohammed, T. A. Ali, and M. H. Aly, "Performance optimization of apodized FBG-based temperature sensors in single and quasi-distributed DWDM systems with new and different apodization profiles," AIP Adv., vol. 3, no. 12, art. 122125, Dec. 2013, doi: 10.1063/1.4859115.
20. H. N. Mandal and S. Sidhishwari, "Optimization and analysis of apodized fiber Bragg grating properties for quasi-distributed sensing," Phys. Scr., vol. 99, no. 7, art. 075504, Jul. 2024, doi: 10.1088/1402-4896/ad4f26.
21. N. Hirayama and Y. Sano, "Fiber Bragg grating temperature sensor for practical use," ISA Trans., vol. 39, no. 2, pp. 169–173, Apr. 2000, doi: 10.1016/S0019-0578(00)00012-4.
22. J. Kumar et al., "Analysis and experiment on simultaneous measurement of strain and temperature by etched and un-etched FBG pair," Results Opt., vol. 5, art. 100135, Dec. 2021, doi: 10.1016/j.rio.2021.100135.
23. H. Qin, P. Tang, J. Lei, H. Chen, and B. Luo, "Investigation of strain–temperature cross-sensitivity of FBG strain sensors embedded onto different substrates," Photonic Sens., vol. 13, no. 1, art. 130117, 2023, doi: 10.1007/s13320-022-0668-3.
24. M. S. E. Djurhuus, B. Schmauss, A. T. Clausen, and D. Zibar, "Simultaneous temperature estimation of multiple gratings using a multi-layer neural network," IEEE Photon. Technol. Lett., vol. 32, no. 19, pp. 1257–1260, Oct. 2020, doi: 10.1109/LPT.2020.3019102.
25. H. N. Mandal and S. Sidhishwari, "Sensitivity analysis of designed apodized fiber Bragg grating sensor using artificial neural network and tree-based models," Results Opt., vol. 10, art. 100343, Jan. 2023, doi: 10.1016/j.rio.2022.100343.
26. P. Khundrakpam et al., "Optical fiber Bragg grating filter for wavelength division multiplexing (WDM) applications," Int. J. Recent Innov. Trends Comput. Commun., vol. 11, no. 10, pp. 2514–2517, Nov. 2023, doi: 10.17762/ijritcc.v11i10.9290.
27. N. A. Mohammed and H. O. El Serafy, "Ultra-sensitive quasi-distributed temperature sensor based on an apodized fiber Bragg grating," Appl. Opt., vol. 57, no. 2, pp. 273–282, Jan. 2018, doi: 10.1364/AO.57.000273.
28. H. N. Mandal and S. Sidhishwari, "Design and optimization of a novel apodization profile of fiber Bragg grating for quasi-distributed sensing network," Opt. Quantum Electron., vol. 54, no. 5, art. 293, May 2022, doi: 10.1007/s11082-022-03691-y.
29. M. H. Aly et al., "A reduced power budget and enhanced performance in a WDM system: A new FBG apodization function," Opt. Quantum Electron., vol. 54, no. 8, art. 471, Aug. 2022, doi: 10.1007/s11082-022-03876-5.
30. A. Barrias, J. R. Casas, and S. Villalba, "A review of distributed optical fiber sensors for civil engineering applications," Sensors, vol. 16, no. 5, art. 748, May 2016, doi: 10.3390/s16050748.
31. G. B. Torres, I. Payá-Zaforteza, P. A. Calderón García, and S. Sales Maicas, "New fiber optic sensor for monitoring temperatures in concrete structures during fires," Sens. Actuators A: Phys., vol. 254, pp. 116–125, Feb. 2017, doi: 10.1016/j.sna.2016.12.013.
32. A. Leal-Junior, A. Frizera, and C. Marques, "Development and characterization of UV-resin coated fiber Bragg gratings," Sensors, vol. 20, no. 11, art. 3026, May 2020, doi: 10.3390/s20113026.
33. Z. Yao, M. Li, G. Li, M. Xing, and N. Chen, "A high-sensitivity fiber Bragg grating sensor for displacement measurement in structural health monitoring," Rev. Sci. Instrum., vol. 94, no. 9, art. 095008, Sep. 2023, doi: 10.1063/5.0156890.
34. B. Sanipatin, L. A. Sánchez, L. Arqués, and S. Sales, "Microsphere-augmented PDMS integration in tapered FBG small-scale sensors for enhanced temperature sensitivity," Sci. Rep., vol. 14, art. 28921, Nov. 2024, doi: 10.1038/s41598-024-80781-9.
35. C. Karapanagiotis and K. Krebber, "Machine learning approaches in Brillouin distributed fiber optic sensors," Sensors, vol. 23, no. 13, art. 6187, Jul. 2023, doi: 10.3390/s23136187.

36. Y. G. Liu, X. Liu, C. J. Ma, and Y. M. Zhou, "Micro-structured optical fiber sensor for simultaneous measurement of temperature and refractive index," Opt. Fiber Technol., vol. 41, pp. 168–172, Mar. 2018, doi: 10.1016/j.yofte.2018.01.019.